Fracture of summer perennial sea ice by ocean swell as a result of Arctic storms

Matthew G. Asplin,[1] Ryan Galley,[1] David G. Barber,[1] and Simon Prinsenberg[2]

[1]   The Arctic summer minimum sea ice extent has experienced a decreasing trend since 1979, with an extreme minimum extent of 4.27×10^6 km^2 in September 2007, and a similar minimum in 2011. Large expanses of open water in the Siberian, Laptev, Chukchi, and Beaufort Seas result from declining summer sea ice cover, and consequently introduce long fetch within the Arctic Basin. Strong winds from migratory cyclones coupled with increasing fetch generate large waves which can propagate into the pack ice and break it up. On 06 September 2009, we observed the intrusion of large swells into the multiyear pack ice approximately 250 km from the ice edge. These large swells induced nearly instantaneous widespread fracturing of the multiyear pack ice, reducing the large, (>1 km diameter) parent ice floes to small (100–150 m diameter) floes. This process increased the total ice floe perimeter exposed to the open ocean, allowing for more efficient distribution of energy from ocean heat fluxes, and incoming radiation into the floes, thereby enhancing lateral melting. This process of sea ice decay is therefore presented as a potential positive feedback process that will accelerate the loss of Arctic sea ice.

Citation: Asplin, M. G., R. Galley, D. G. Barber, and S. Prinsenberg (2012), Fracture of summer perennial sea ice by ocean swell as a result of Arctic storms, *J. Geophys. Res.*, *117*, C06025, doi:10.1029/2011JC007221.

1. Introduction

[2]   Dramatic reductions in sea ice thickness [*Rothrock et al.*, 1999; *Hilmer and Lemke*, 2000], age of ice [*Maslanik et al.*, 2007; *Nghiem et al.*, 2007; *Maslanik et al.*, 2011], volume [*Kwok et al.*, 2009], and an increasing melt season length [*Markus et al.*, 2009] have been observed in the northern hemisphere. The passive microwave record from 1979–2010 shows a decline in summer minimum Arctic sea ice extent at a rate of approximately 81,310 km^2 year^{-1} (12.4% decade $^{-1}$) [*Stroeve et al.*, 2011a]. A trend in multiyear (MY) ice loss by in situ melting in the Southern Beaufort Sea has been identified [*Kwok and Cunningham*, 2010] and the oldest types (5 years and older) of sea ice have all but disappeared comprising only 3.04×10^5 km^2 (10%) of remaining MY Arctic sea ice in 2010 [*Maslanik et al.*, 2011]. These phenomena are attributed to increasing regional air temperatures and increased summer ocean mixed layer temperatures [*Intergovernmental Panel on Climate Change*, 2007; *Stroeve et al.*, 2011a] coupled with wind-forcing of sea ice [*Ogi et al.*, 2010], persistence of the Beaufort Sea high during summer, increased ocean heat

fluxes [*Shimada et al.*, 2006; *Woodgate et al.*, 2006; *Steele et al.*, 2008], and increased surface solar heating [*Perovich et al.*, 2008]. Due to the decline of sea ice extent, large open-water anomalies have been observed in the Chukchi, Siberian, Laptev, and Beaufort seas in 2007–2010, as well as large areas of heavily decayed first-year (FY) and MY sea ice [*Barber et al.*, 2009] have been observed.

[3]   The observed rapid reduction of summer sea ice extent and decreasing regional albedos highlight the importance of ocean heat fluxes. Two important ocean heat processes to consider are increasing rates of advective ocean heat transfer from lower latitudes, and increases in solar heating of the ocean surface. An increase of total heat flux into the Arctic through the Bering Strait identified by *Woodgate et al.* [2006] between 2001 and 2004 is capable of melting 640,000 km^2 of 1-m-thick ice, which matches the reduction in sea ice extent in September ($\sim$700,000 km^2) for the same period. *Steele et al.* [2008] identifies an average increase in the upper ocean heat content of the summertime southern Chukchi and western Beaufort Seas of about 50 MJ m^{-2} decade^{-1} during 1965–1995 (150 MJ m^{-2} over 30 years). *Perovich et al.* [2008] investigates solar heating 1979–2005 in the northern Chukchi Sea and identifies an average increase of 200 MJ m^{-2}.

[4]   The declining extent of Arctic sea ice is statistically linked to increasing latent heat fluxes to the atmosphere [*Simmonds and Keay*, 2009; *Stroeve et al.*, 2011b]. Increased latent heat fluxes are purported to be linked to a concurrent increase in Arctic cyclone intensity [*Simmonds and Keay*, 2009; *Higgins and Cassano*, 2009]; however, a recent study by *Stroeve et al.* [2011b] indicates that this linkage is not yet clear. Storms that form over Eastern Siberia during the summer and autumn can migrate into the Chukchi and Beaufort

[1]Center for Earth Observation Science, Faculty of Earth, Environment and Resources, University of Manitoba, Winnipeg, Manitoba, Canada.
[2]Bedford Institute of Oceanography, Department of Fisheries and Oceans Canada, Bedford, Nova Scotia, Canada.

Corresponding author: M. G. Asplin, Center for Earth Observation Science, Faculty of Earth, Environment and Resources, University of Manitoba, Winnipeg, MB R3T 2N2, Canada. (asplinm@cc.umanitoba.ca)

Seas [*Serreze and Barry*, 1988; *Zhang et al.*, 2004]. Cyclones that become coupled to the cold polar vortex aloft may persist for several weeks [e.g., *LeDrew et al.*, 1991], and cyclone winds can even reverse the rotational circulation of the Beaufort Sea Ice Gyre [*McLaren et al.*, 1987], which can lead to divergence in the pack ice [*Proshutinsky et al.*, 2002]. This process leads to fracturing within the pack ice, thereby affecting regional albedos and thermodynamic sea ice processes [*Stroeve et al.*, 2005]. Changes in summer precipitation from Arctic cyclones may also be contributing to summer sea ice decline. Summer Arctic precipitation occurring as rain (snow) has increased (decreased) by 40% over the period 1989–2009, thereby resulting in less snow covered summer sea ice and decreased regional albedos [*Screen and Simmonds*, 2011].

[5] The interaction of strong winds from persistent, intense Arctic summer cyclones with increased fetch distances introduces the potential for swells to originate within the Arctic basin. Waves propagating through sea ice are attenuated by viscous losses, scattering interactions between leads and pressure ridges [*Wadhams*, 1973], and their amplitudes are attenuated exponentially with an exponent of 3 [*Squire et al.*, 2009]. However, wave trains containing long waves can propagate far into the pack ice. Analysis of ocean wave train evolution and propagation in a 1670 km-long profile of irregular Arctic sea ice obtained from a submarine transect shows that ocean waves with period of 22 s can propagate through the ice cover, and waves with period of 17 and 13 s penetrate 350 km and 80 km respectively [*Squire et al.*, 2009]. Long wave propagation has previously been documented deep in the Arctic pack ice [*Hunkins*, 1962*; Liu and Mollo-Christensen*, 1988], and corresponds with measurements showing low-amplitude (sub-mm) oscillations in ice floes and ice islands at wave periods of 15–60 s [*Wadhams and Doble*, 2009].

[6] Long waves propagating through Antarctic sea ice have been observed to cause flexural swell and fracture within the sea ice cover [*Wadhams et al.*, 1988]. This process has been observed to fracture Antarctic sea ice into smaller, mobile floes that are more susceptible to lateral melting and dynamic forcing [*Toyota et al.*, 2006; *Steer et al.*, 2008]. The minimum size of a resultant ice floe depends on the ice thickness of the parent floe, where minimum floe diameters after breakup of 14, 24, and 33 m are identified for 1, 2 and 3 m parent ice floe thicknesses respectively [*Mellor*, 1986]. Flexural swell is most effective at causing fracture within large, contiguous ice floes, and may not affect smaller floes at all [*Rothrock and Thorndike*, 1984]. Fracturing of sea ice depends highly on the ice floe physical properties, where ice temperature, salinity, and strength are interrelated [*Frankenstein and Garner*, 1967; *Timco and O'Brien*, 1994; *Timco and Johnston*, 2002].

[7] In this paper, we present in situ observations of large swell propagation into MY Arctic sea ice, and (what we believe to be) first-ever observations of simultaneous fracturing of thick, MY sea ice floes. We determine the origins of the swell, and discuss the physical implications of flexural failure on MY Arctic sea ice dynamic and thermodynamic processes. Because of the recent increase in the open water in summer, this swell induced fracturing may now be a

significant feedback mechanism, increasing sea ice decay in the Arctic Ocean.

2. Data and Methods

[8] In situ observations of the atmosphere-sea ice-ocean system in the southeastern Beaufort Sea were made from the Canadian Coast Guard Research Icebreaker (CCGS) *Amundsen*. The case study presented here is extracted from the joint ArcticNet/IPY–GeoTraces project, which took place between 27 August and 12 September 2009. The objectives of the ice program during this period were to investigate the geophysical characteristics of the summer ice and to study how sea ice responds to thermodynamic and dynamic forcing.

[9] Canadian Ice Service (CIS) digital ice charts were employed for real-time ship and science operations planning during the cruise. CIS digital ice charts are based on expert manual interpretation of Radarsat-1 data (the primary data source since 1996), NOAA-AVHRR and Envisat ASAR data and in situ aerial and marine surveys. They include total sea ice concentration and partial concentrations by development stage.

[10] Sea ice thickness surveys were made using a helicopter-mounted electromagnetic induction (EMI) system. This system is well established [e.g., *Prinsenberg and Holladay*, 1993] and consists of the electromagnet, a laser profiler, a nadir-facing video system and navigation, control and archive systems. The near-circular footprint of the helicopter EMI system is about 2.5 times the altitude at which it is flown (∼4–6 m). The nadir-looking digital camera acquired video of the sea surface from 130 m of altitude. The video width is at a 1 to 1 ratio with altitude. We use this ratio to manually estimate ice floe diameters on video images prior to and after the flexural fracture event. The distribution of ice floe diameters is then fitted to a power law curve to create two sea ice floe-size cumulative number distributions which can subsequently be used to calculate the change in sea ice floe perimeter.

[11] The distribution of ice floe sizes typically follows a cumulative number distribution that behaves like a power law relationship (equation (1)) that can vary from year to year and by region [*Rothrock and Thorndike*, 1984]:

$$N(d)_i \propto a d_i^k \qquad (1)$$

where $N(d)$ is the cumulative number distribution for floe size regime i, k is the scaling exponent, and a is a constant. Recent studies identify distinct floe size regimes with their own distinct power law distributions [*Toyota et al.*, 2006; *Steer et al.*, 2008]. *Toyota et al.* [2006] identify two distinct ice floe size distributions: 0–40 m diameter, and >40 m. *Steer et al.* [2008] describes floe size distributions during the Ice Station Polarstern program (ISPOL), and three distinct distributions are identified for ice floe size: 2–20 m, 20–50 m, and >50 m. Each distribution follows a power law distribution with its own unique exponent k.

[12] MY ice was physically sampled at station L1 on 31 August 2009 (Figure 1), and heavily decayed first-year (FY) ice station L2 on 04 September 2009 (Figure 1) using a

a 04 September 2009 - Sea ice extent
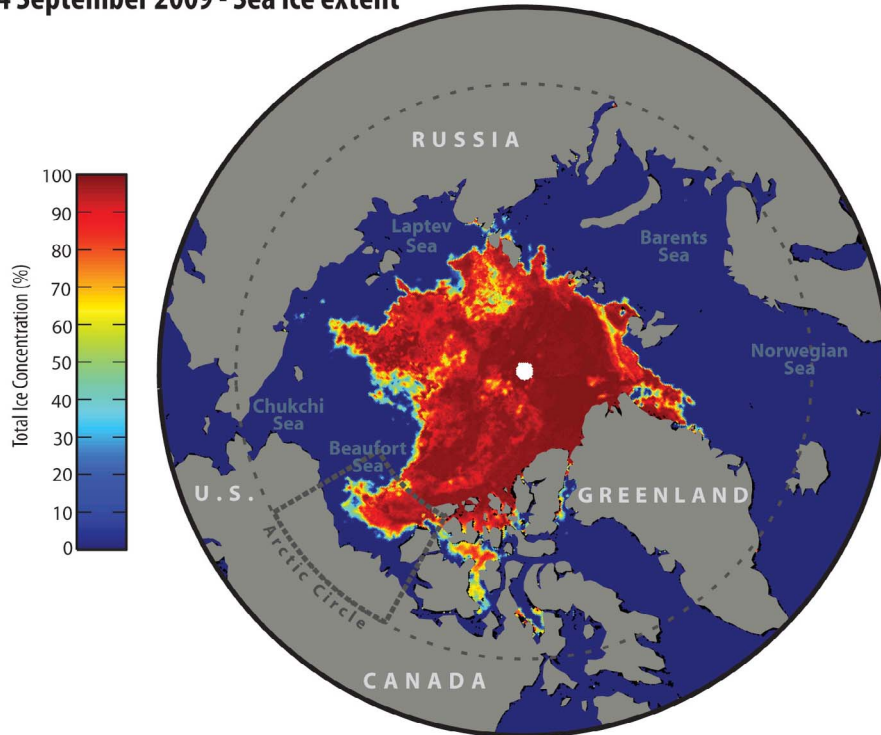
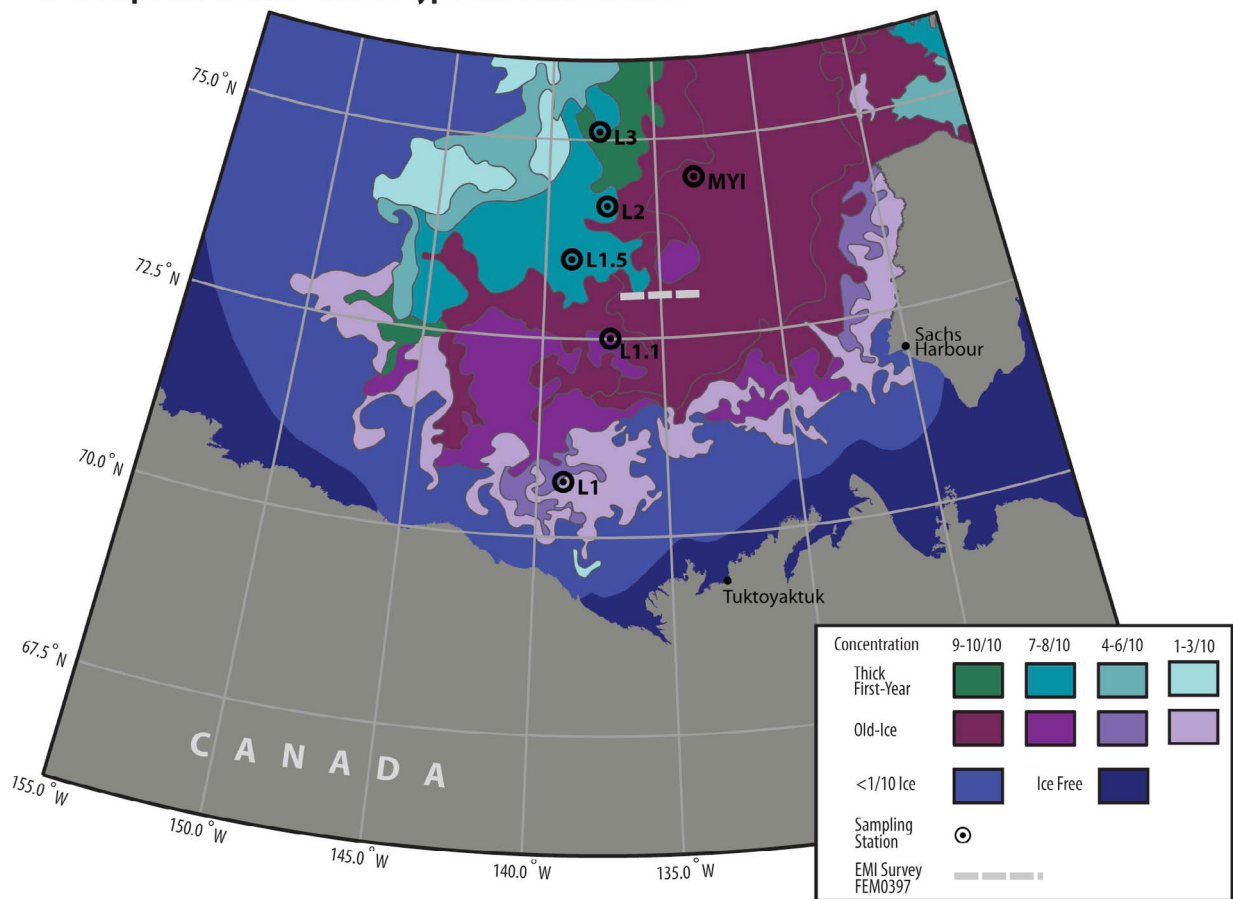## b 07 September 2009 - Sea ice type and concentration

Figure 1

Kovacs Mark II coring system. Sea ice temperature profiles were measured immediately after extracting the ice core by placing a temperature probe in holes drilled at 10 cm intervals beginning at 5 cm from the sea ice surface. Sea ice salinity was measured by cutting a second core into 10 cm sections, placing them in sealed buckets and melting them. Salinity of the melt was calculated from conductivity and temperature using a HACH SENSION5 portable conductivity meter. Sea ice thickness was measured in situ with a measuring tape. A conductivity-temperature-depth (CTD) profile of the near-surface ocean column was made from the ship's zodiac using an Idronaut Ocean Seven model 304 CTD.

[13] Meteorological data including sea level pressure, air temperature, relative humidity, and vector winds were collected with an AXYS Automated Voluntary Observation System (AVOS), located on the roof of the ship's wheelhouse. Cloud heights were measured using a Vaisala CT25K ceilometer, mounted directly behind the wheelhouse on the port side of the ship. Cloud fractional cover was assessed manually every three hours, and later compared with imagery from an all-sky camera system, consisting of a Nikon D-90 camera with an upward-looking fisheye lens. Downwelling long wave ($L\downarrow$) and shortwave radiation ($K\downarrow$) were collected using an Eppley PIP pyrgeometer and a PSP pyranometer mounted on top of the wheelhouse. A Radiometrics TP/WVP 3000A microwave radiometer profiler (MWRP) measured atmospheric temperature and absolute humidity to a height of 10 km. Temperature and humidity values were derived from microwave brightness temperatures using the manufacturer's neutral network retrievals trained with rawinsonde measurements, and a radiative transfer model [*Solheim et al.*, 1998].

[14] Daily and six-hourly gridded atmospheric data were retrieved from archives maintained by the NOAA-CIRES Climate Diagnostics Centre (CDC), which originate from the National Center for Environmental Prediction (NCEP) Reanalysis I Project [*Kalnay et al.*, 1996]. The spatial resolution of these data is a $2.5° \times 2.5°$ (latitude and longitude) grid. Daily composites of mean sea level pressure (MSLP) and mean vector winds are created for 01–06 September 2009 to show the development and movement of cyclones, and resulting surface winds. It should be noted that the accuracy of NCEP Reanalysis I project MSLP and daily scalar wind data is poor, and must be accounted for when interpreting analysis results. *Bromwich and Wang* [2005] compare Arctic rawinsonde wind measurements obtained as part of the CEAREX project with NCEP reanalysis I data, and show that average magnitudes of u and v component winds are understated by NCEP reanalysis I. Correlation coefficients between observed and NCEP reanalysis I data for u and v of ($r = 0.24$ and $r = 0.63$ respectively) show that v component winds are better represented than u component winds; however, it is clear that there is considerable error in both fields.

[15] We were able to directly measure heave, pitch and roll on the *Amundsen* during the swell propagation event while at the MYI and L3 stations (Figure 1), using an Applanix POSMv 320 v4 3-D motion sensor, with a sampling frequency of 100 Hz. It should be noted that ship heave depends on ship-hull characteristics and does not provide a direct measure of wave properties; however given the long wavelengths of the observed swells, we are able to obtain reasonable averaged estimates of wave amplitude and period. We then use our estimates of wave amplitude and period to calculate wavelength and wave phase velocity. In deep water, wavelength and period are related by equation (2):

$$\lambda = \frac{gt^2}{2\pi} \qquad (2)$$

where λ is wavelength (m), t is wave period (sec), and g is gravitational acceleration (9.81 m s^{-2}) [*Bearman*, 1999, pp. 12–47]. Wave phase velocities are half the average velocity of the actual waves within a wave train, and therefore the energy associated with these waves travels at the wave phase velocity. Deep water wave phase velocity c (m · s^{-1}) follows as equation (3):

$$c = \frac{\lambda}{2t} \qquad (3)$$

[16] Based on the wave phase velocity and direction of the longest wavelength wave groups, we were able to estimate an origin time and location of the swell.

[17] Sea ice flexural strength can be related to the brine volume or total porosity of the ice where increasingly porous ice will have a corresponding decline in ice strength [*Timco and O'Brien*, 1994]. The flexural strength of sea ice in MPa (σ_f) can be described by

$$\sigma_f = 1.76e^{-5.88\sqrt{v_b}} \qquad (4)$$

where v_b is expressed as a brine volume fraction. The brine volume of sea ice can be related to ice temperature (T_i) and ice salinity (S_i) [*Frankenstein and Garner*, 1967].

$$v_b = S_i\left[\frac{49.185}{T_i} + 0.532\right] \text{for} -0.5°C \geq T_i \geq -22.9°C \qquad (5)$$

3. Results

[18] On 04 September 2009; we expected the CCGS *Amundsen* to enter summer MY sea ice cover at about 71.333°N, 139.00°W where we had planned to follow a south-to-north transect penetrating as far north into the pack ice as conditions would allow (Figure 1). The CIS chart for 07 September 2009 indicated 7 to 9 tenths old and MY sea ice cover, increasing to 9+ tenths cover as we progressed northward along our sampling line; however, we only encountered heavily decayed FY ice interspersed with fragments of MY ice along this route. This sea ice cover encompassed a large area in lieu of expected MY sea ice, and has been described in detail in *Barber et al.* [2009].

[19] The lack of MY sea ice required us to alter our cruise plan. On 06 September, the CCGS *Amundsen* headed

---

Figure 1. (a) National Snow and Ice Data center (NSIDC) sea ice areal extent; (b) Canadian Ice Service ice chart for 07 September 2009 showing sea ice concentration and stage of development. Ship-based sampling sites and EMI survey FEM09397, flown on 09 September 2009, are shown.
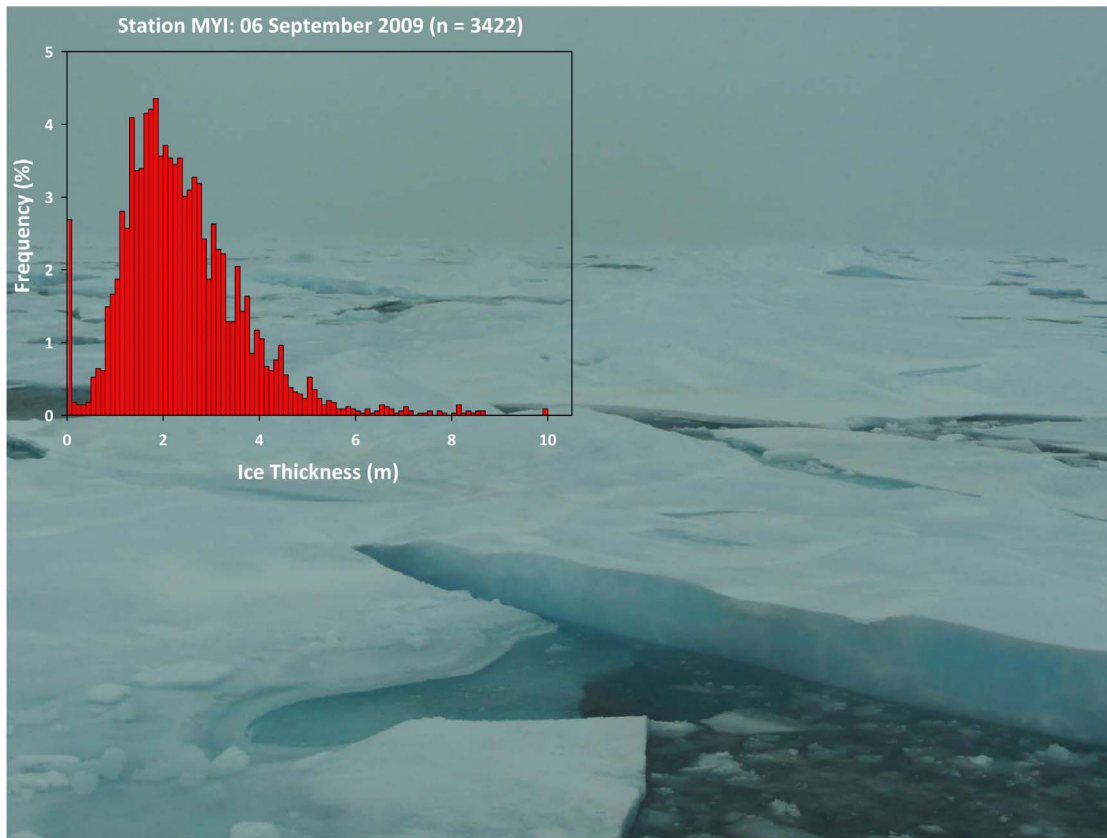
Figure 2. Summary of 06 September 2009 afternoon helicopter EMI survey (FEM09381) flown over, multiyear ice floes at station MYI. The image shows a thick (∼5 m) multiyear ice floe after flexural fracture as observed from the wheelhouse of the ship. The histogram shows a distribution of ice thicknesses with a mean of 2.0 m.

eastward toward the Queen Elizabeth Islands, a region with a high likelihood of large, thick MY ice floes. We progressed through the heavily decayed ice region into a transitional region containing a mix of decayed old and FY sea ice floes, and finally into thick late summer MY pack ice. Using the onboard helicopter to survey the area, we identified a vast MY floe (∼10 km diameter), to which we intended to moor the ship, and conduct our typical science operations. The ice in this area was much thicker than the heavily decayed FY ice we that we had encountered the previous day to the west. Our helicopter EMI system recorded overall thicknesses of sea ice around station MYI (e.g., mean = 2.0 m, max = 10 m) (Figure 2).

[20] As ice teams initially prepared to deploy to the ice, we noticed the appearance of a swell from the ships helicopter deck. Laser data collected during the helicopter EMI survey at station MYI indicated a swell period of 13.5 s, and a wavelength ranging from 200–300 m (Figure 3). Laser data were collected while the helicopter hovered over a large MY ice floe. These data were augmented with three-dimensional dynamic ship positioning data, which revealed approximate ship heave amplitude of 0.4 m, also with a period of 13.5 s. The swell caused the vast MY ice floe nearest the *Amundsen* to ride up one side of the swell and fracture as it crested the wave peak, creating smaller ice floes of width approximately one half of the wavelength of the swell. In a matter of minutes from the initial onset of swell propagation, all large MY

ice floes in the region were fractured in this manner, yielding a new distribution of smaller MY ice floes ranging from 100–150 m in diameter. A helicopter-borne video system recorded this event in still photographs along its flight track which were later combined to create a series of photo mosaics (Figure 3). Photos of the fractured MY ice floes were also taken from the ship wheelhouse (Figure 2).

[21] Upon completion of the helicopter-borne EMI and video surveys, the region of heaving MY sea ice cover was deemed unsafe to work on, and the *Amundsen* sailed west to continue regular science operations in areas of lower sea ice concentration (Station L3, 75.3341°N, 137.704°W). On 07 September 2009, we observed swells of shorter period (∼9 s) and amplitude of ∼0.8 m. On 09 September 2009, we conducted a longitudinal helicopter EMI survey at 72.5°N (Figure 4), and determined the limit of the swell penetration into the pack ice at 72.526°N 134.51°W, a penetration of 350 km. Furthermore, the rotted FY ice margin was heavily fractured, with small floe sizes ranging from 20–50 m in diameter (Figure 4).

[22] MSLP for the period 01–06 September 2009 revealed the development of two large low-pressure systems (cyclones) over the Siberian coastline on 01 and 04 September 2009, with minimum central pressures of 990 mb and 986 mb respectively (Figure 5). Both cyclones were coupled to the polar vortex and steered toward the northeast, tracking over the Chukchi and Beaufort Seas. Mean daily surface
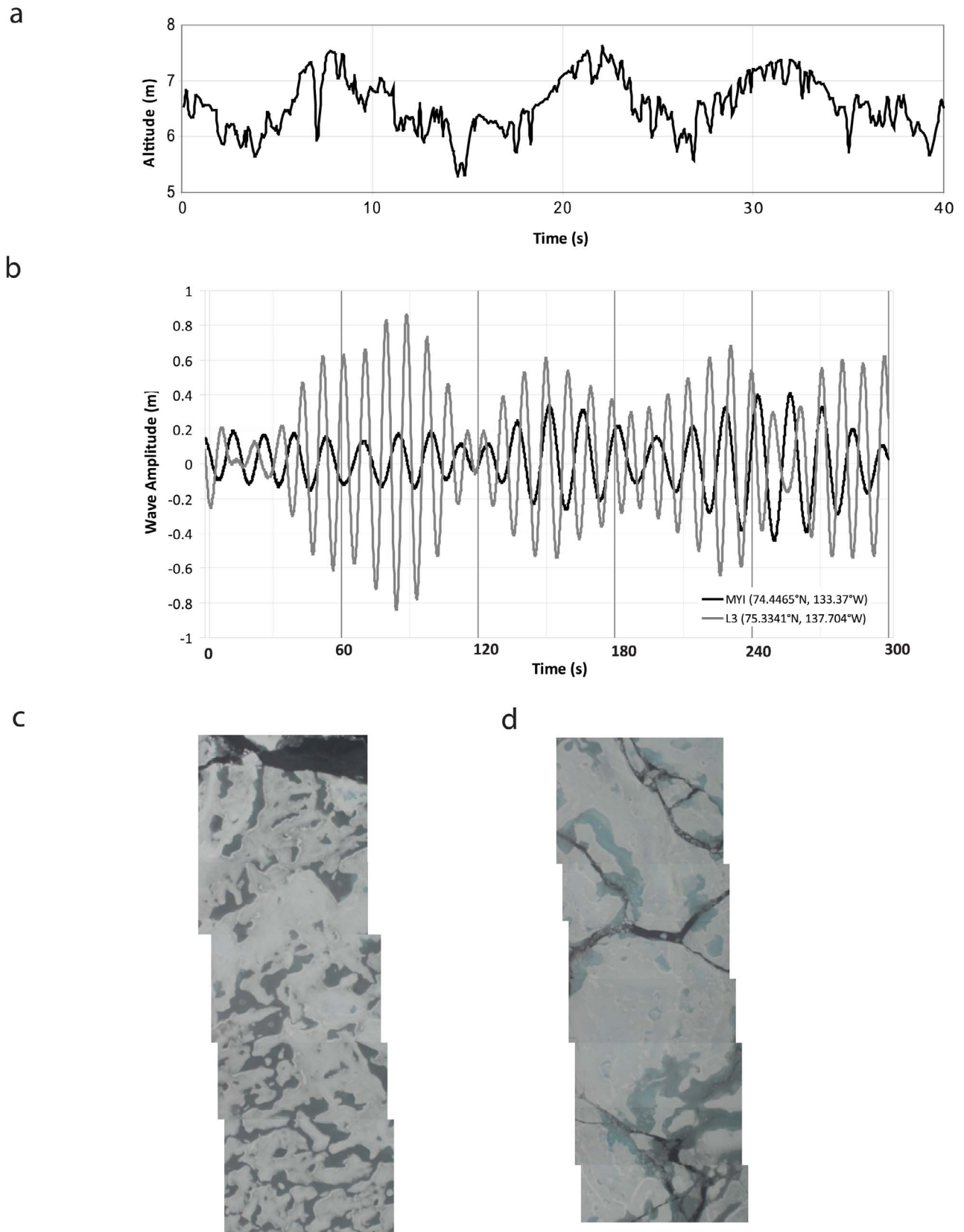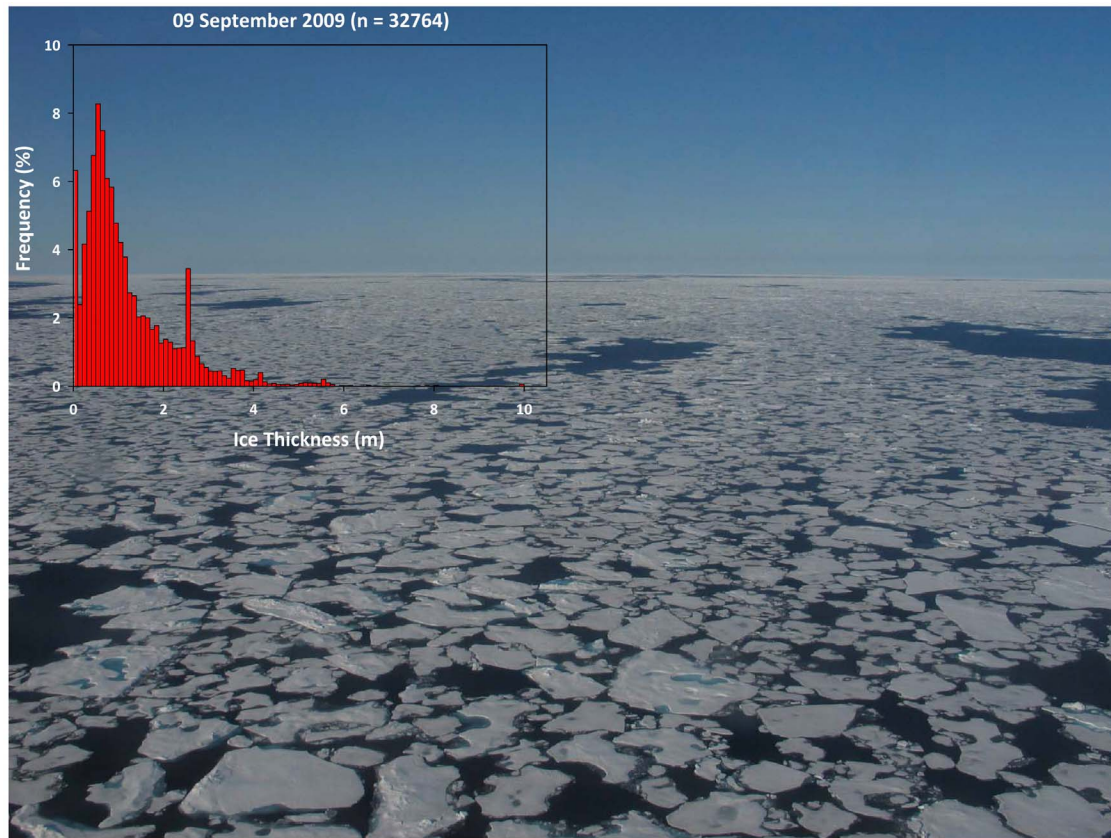
a

b

c

d

Figure 3

Figure 4. Summary of 09 September 2009 afternoon long-line (FEM09397) helicopter EMI survey flown over fractured first and second-year ice floes from 72.52°N 136.75°W to 72.52°N 133.40°W. Image shows rounded first-year ice floes ranging in diameter from 20–50 m as observed from the helicopter survey. The histogram describes the ice thickness distribution with a bi-modal distribution with peaks at 0.8 m and 2.5 m.

winds were calculated for 01–06 September 2009 (Figure 5). Of particular interest are the winds from the 04 September cyclone, which deepened rapidly on 04–05 September 2009 along the Siberian coast. This storm produced strong west and west-southwest winds averaging 12–$14 \, \mathrm{m \cdot s^{-1}}$ from 04–05 September 2009. Spot wind analysis for 12Z 05 September 2009 (not shown) indicates wind speeds may have been gusting to $20 \, \mathrm{m \cdot s^{-1}}$.

[23] Westerly winds from the two cyclones interacted with the large wind-fetch associated with the ice free Chukchi and Siberian Seas, and forced the development of swells. Using our predetermined periods of 13.5 s and 8.5 s, and wavelengths of 285 m and 150 m, we calculate wave phase velocities of $11 \, \mathrm{m \cdot s^{-1}}$ and $6.81 \, \mathrm{m \cdot s^{-1}}$ respectively. We estimate that the center of the storm was 970 km from station MYI, thereby yielding a travel time for wave groups of 24.5 and 39.5 h respectively. This indicates that the swell development was driven by winds from the 04 September 2009 cyclone, with the waves groups containing the longest wavelengths traveling the fastest.

[24] The strength of sea ice played a key role in permitting the penetration of the swell into the pack ice, and to its flexural fracture. Sea ice strength was assessed by examining temperature and salinity profiles from physical ice core samples (Figure 6). By applying equations (4) and (5), we calculate the average flexural strength to be 64.3 kPa for the FY ice at station L2 and 40.9 kPa for the MY ice at station MYI. These values reflect weak and brittle sea ice and are in agreement with typical late-summer values which can range from 30–60 kPa [*Timco and Johnston*, 2002]. The weak sea ice conditions are attributed to well-drained ice profiles and nearly isothermal temperature profiles. Temperature values from both ice core samples show nearly isothermal temperature profiles. In addition, MWRP temperature values for the atmosphere near the surface were ~0°C, indicating that the sea ice and atmosphere are nearly in thermal equilibrium. The CTD ocean profile shows clear stratification near the surface where cold, fresh meltwater (salinity of 27, and temperature of −1.4°C) lies above a mixed layer (salinity >28, and temperature of −1.25°C–1.0°C).

Figure 3. (a) Laser altimeter data from the EMI system at 13:30LST. (b) Example of 100 Hz ship heave while at station MYI (06 September 2009, 18:00 to 18:05 UTC) and at station L3 (07 September 2009, 13:40 to 13:45 UTC). (c) 17:02 UTC from 06 September 2009 at station MYI, video width = 140. No cracks in old, 2 m thick ice floe are visible. (d) 19:00 UTC 06 September 2009. Thick ice (2 m thick in level ice sections) at station MYI now has cracks aligned perpendicular to swell direction running from NW to SE. Crack spacing is approximately the width of the video (110 m).
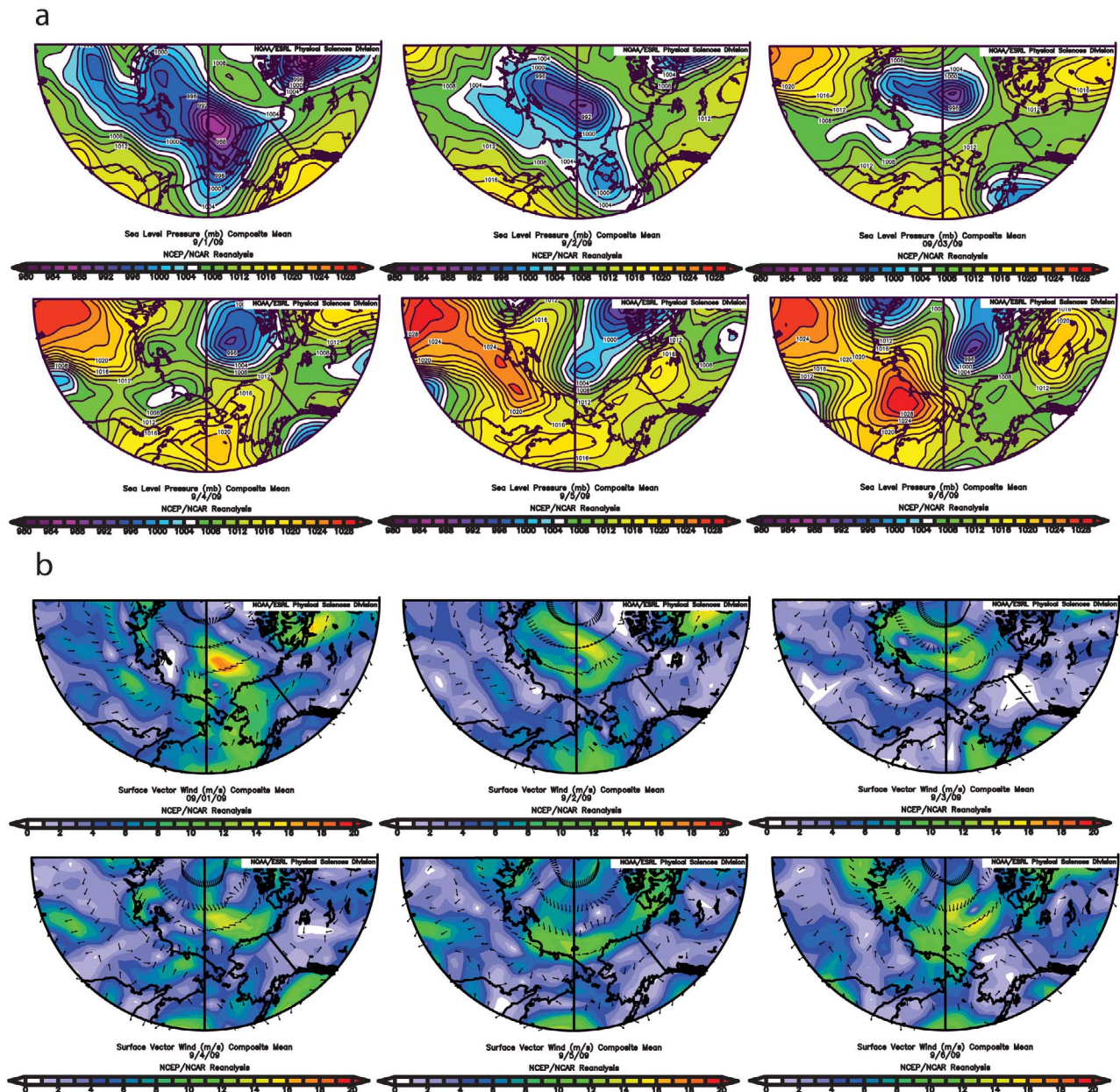
Figure 5. Daily composites for 01–06 September 2009. (a) MSLP (mb); (b) daily mean vector wind (m/s). (Images provided by the NOAA/ESRL Physical Sciences Division, Boulder Colorado from their Web site at http://www.cdc.noaa.gov/).

[25] After the ∼10 km MY ice floe underwent the observed flexural failure event, a helicopter-borne aerial assessment of the regional ice cover revealed a distribution of ice floe diameters ranging from 100–150 m. Ice floes in the FY ice were reduced from ∼1 km in size to 20–50 m. These small floes are difficult to break mechanically and therefore distributions of small ice floes are governed primarily by thermodynamics [Mellor, 1986]. Sea ice concentration in the 'rotten' FY ice zone [Barber et al. 2009] was observed at eight-tenths coverage on 07 September 2010, a decrease of one-tenth from prior to the event.

[26] In situ observations of cloud cover, K↓ and L↓ are used to characterize the surface radiation budget for

06 September 2009 (Figure 7). Two distinct cloud layers were detected throughout the day at an average height of 550 m and 3000 m respectively. Cloud-fraction cover initially was 75% and became 100% at 06:00 UTC. K↓ initially was 167.5 W·m^{-2} (hourly average for 00:00–01:00 UTC), 0 W·m^{-2} from 05:45–12:20 UTC and then reached an hourly average intensity of 79.9 W·m^{-2} by 23:00 UTC. The daily average value of L↓ at the surface was 307.4 W·m^{-2}.

4. Discussion

[27] The long wave swells responsible for the flexural failure in the MY sea ice are due to two key environmental factors. First, the increased fetch across the open water in the
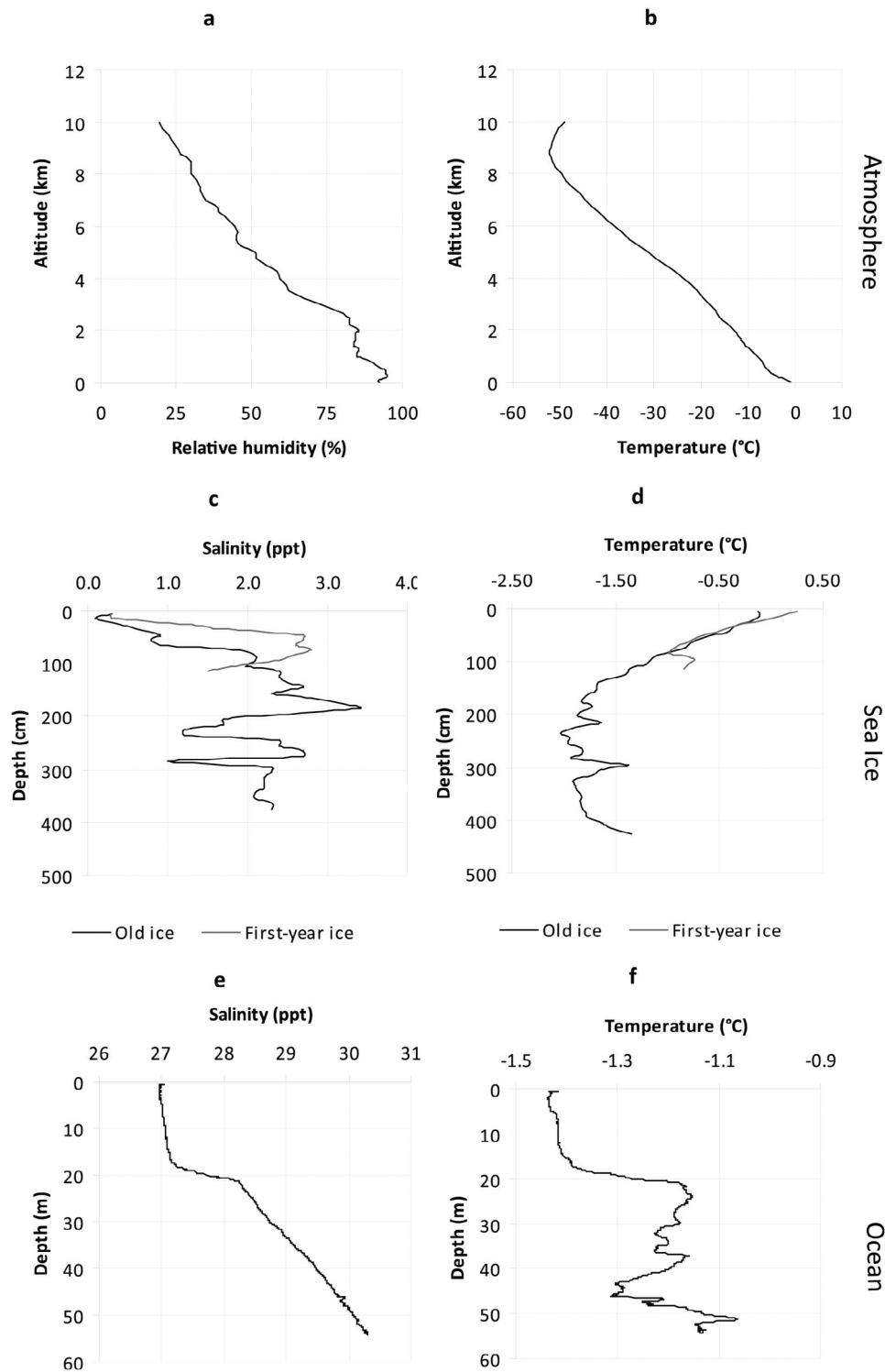
Figure 6. Isothermal environment and sea ice. (a) Atmospheric relative humidity and (b) temperature profiles for 06 September 2009. (c) Ice salinity (d) and temperature profiles for old ice and heavily decayed first-year ice taken at stations MYI and L2. (e) 0–50 m ocean salinity and (f) temperature profiles taken at station L2.

East Siberian and Chukchi Seas permits migratory Arctic cyclones to generate large waves and swells within the Arctic Ocean. Second, the heavily decayed ice margin did little to attenuate the large swells, and allowed them to penetrate 350 km into the pack ice in the Southern Beaufort Sea. The available fetch (coastline-to-ice edge) was on the order of 1800 km. Strong west-southwest winds associated with the slow-tracking 04 September cyclone persisted over
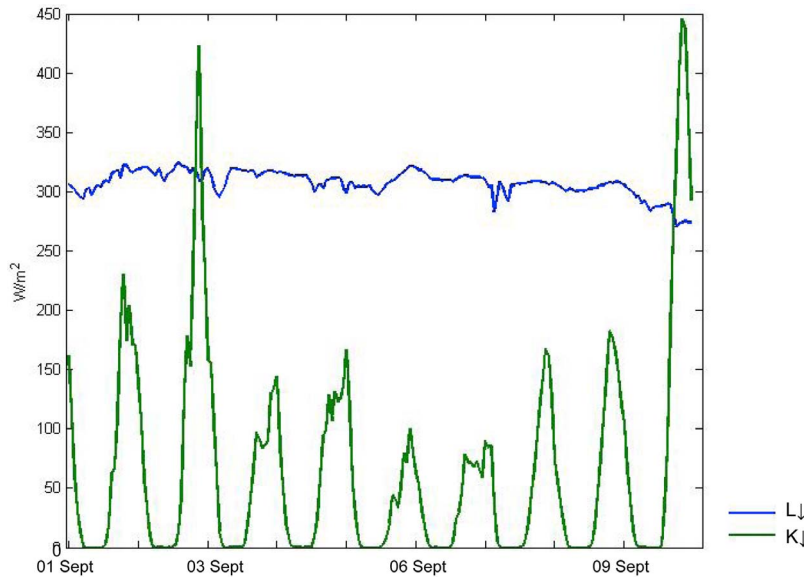
Figure 7. Incoming shortwave (K↓) and longwave (L↓) radiation time series measured from the CCGS *Amundsen* from 01–09 September 2009.

the predominantly ice-free Chukchi and Siberian Seas for at least 36 h. Winds from this cyclone appear to have built upon pre-existing sea state conditions generated by strong winds from the 01 September cyclone, thus a lesser duration of strong winds was required to build a fully developed sea state. The travel time for the long wave packets observed at station MYI from their place of origin is estimated at 24.5 h, thereby indicating that the 04 September storm was the source of the long waves.

[28] Fracturing of sea ice due to wind stress, or wave stress depends greatly on sea ice strength. The physical strength of a sea ice floe depends on its internal temperature [*Timco and O'Brien*, 1994; *Tison et al.*, 2009], with decreasing compressive strength with increasing temperature of the ice. Ice floe properties and ice floe distributions in a given region are dependent on the mechanical and physical properties of the surrounding sea ice [*Tison et al.*, 2009]. It is apparent that deteriorated ice strength attributed to summer warming [*Eicken et al.*, 1995] played a critical role in the flexural failure of the MY ice floes at station MYI. Furthermore, the heavily decayed ice edge margin [*Barber et al.*, 2009] represents a very weak ice cover that did little to attenuate the incoming swell.

[29] To better estimate the post-flexural failure potential rates of lateral melt, we follow the analysis conducted by *Toyota et al.* [2006] to investigate the influence that an increasing distribution of smaller floe sizes has on lateral melting within the fractured MY pack ice in our study region. The technique involves estimating total ice floe perimeter before and after the occurrence of flexural failure, using ice floe size distributions from prior-to and following the penetration of the long wave swell. Floe diameters are set to range from 150–1500 m and 40–150 m before and after the event respectively. Ice floe size distributions are derived following and prior to the flexural failure event with power law exponents of $k_1 = 1.35$ and $k_2 = 1.93$ respectively. Our values of k are comparable with earlier studies. *Rothrock and Thorndike* [1984] estimated values of k for ice floes greater

than 100 m of $1.7 < k < 2.5$, and k = 1.11 for ice floe distributions <40 m. Our value of $k_1 = 1.93$ for ice floe sizes of >150 m is comparable to that found by *Rothrock and Thorndike* [1984]. Our value of $k_2 = 1.35$ for ice floe sizes of 40–150 m is reasonable, given that the value of k increases with mean floe size.

[30] Following *Toyota et al.* [2006], the integration is evaluated against a fixed sea ice concentration ($A = 0.8$) in equation (6):

$$A = \int_{d_1}^{d_2} n_a(x)s(x)dx + \int_{d_2}^{d_3} n_b(x)s(x)dx \qquad (6)$$

[31] Evaluating the integral gives equation (7):

$$A = -\frac{\pi\beta k}{4(k-2)}\left(d_2^{-k_1+2} - d_1^{-k_1+2}\right)$$
$$-\frac{\pi\beta k}{4(k-2)}\left(d_3^{-k_2+2} - d_2^{-k_2+2}\right) \qquad (7)$$

where $d_1 = 40$ m, $d_2 = 150$ m, $d_3 = 1500$ m are floe diameters (the upper and lower sizes before and after the event), $n_a(x)dx$ are the number of floes whose diameters are x to $x + dx$ per unit area, $s(x)$ is area of a floe ($\pi d^2/4$), and β is a coefficient for the power law distribution. Assuming approximately rounded floes, this exercise estimates that total ice floe perimeter immediately following flexural failure is approximately 4.5 times greater than before. The actual increase in floe perimeter is likely less as we assume round ice floes, when in fact many of the floes are elliptical or rectangular.

[32] It is expected that flexural failure of MY sea ice, and a corresponding decrease in mean floe diameter size would affect thermodynamic forcing upon sea ice mass balance. Reductions in mean ice floe diameter results in approximately 4.5 times increase in ice floe perimeter exposed to the ocean, thereby increasing lateral melting via ocean heat flux. The concurrent reduction of sea ice concentration will

decrease the regional albedo, resulting in increased entrainment of L↓ and K↓ to the ocean surface, also enhancing rates of lateral melt. Lateral melting becomes dominant for floes less than several hundred meters in diameter [*Steele*, 1992], and floes <40 m in diameter are highly susceptible to lateral melting [*Toyota et al.*, 2006]. *Steer et al.* [2008] attributed a significant increase in the number of small floes (<100 m) over a 23-day period in the western Weddell Sea during the ISPOL program to wave-forced divergence in the pack ice, followed by lateral melt. Lateral melting in these areas is likely enhanced due to efficient radiation entrainment in surrounding waters, and a marked increase in initial total ice floe perimeter [*Toyota et al.*, 2006; *Steer et al.*, 2008]. It is also expected that smaller mean floe sizes combined with increased ocean heat fluxes via increased solar surface heating [e.g., *Perovich et al.*, 2008], and ocean heat advection [e.g., *Woodgate et al.*, 2006], may also enhance the efficiency of bottom-melting. Small ice floes are also more susceptible to dynamic forcing from the wind and ocean currents in the area. They may become easily entrained into the Beaufort Gyre, and moved toward the Chukchi Sea, and Bering Strait where they would be exposed to enhanced ocean heat fluxes from Pacific water intrusions through the Bering Strait [*Shimada et al.*, 2006; *Woodgate et al.*, 2006; *Perovich et al.*, 2008], and would also be vulnerable to wave-induced melt as described by *Wadhams et al.* [1979].

[33] This process may also have several dynamical implications for the autumn freezeup period. Small MY ice floes that survive the summer may actually promote ice growth and ice thickness redistribution through rafting and ridging of young FY ice types. Conglomerate ice floes containing young FY ice and small MY ice floes are likely to be initially more susceptible to breakup during freezeup season which may enhance sea ice mobility and increased ice ridging during the early stages of the freezeup season. As freezeup progresses, this process may actually increase ice pack stability where ice thicknesses have increased due to ridging and dynamic ice growth. The impacts of this process on freezeup processes therefore warrant investigation as this may represent a positive feedback on ice growth.

[34] If this event is analogous to the ongoing wind-wave forcing described by *Steer et al.* [2008], we expect the distribution of ice floes to shift rapidly toward small diameter ice floes. Although the event occurred close to the 12 September 2009 minimum summer Arctic sea ice extent, measured values of K↓ and L↓ radiation suggest that sufficient net radiative energy was available at this particular latitude to drive melting for a period following our departure. 80% of the net thermal energy that enters the ocean through leads goes toward melting ice, while the rest warms the ocean [*Steele*, 1992]. The decrease in mean surface albedo following fracture would allow the ocean surface to absorb a greater amount of incoming radiation, which then would drive lateral melting in the ice floes. Furthermore, ocean heat fluxes would also continue to drive bottom melting.

5. Conclusions

[35] The mechanical sea ice decay process described in this paper is presented as the result of a combination of several dynamical environmental factors: (1) Reduced summer sea ice extent results in a large area of open water providing a long fetch, (2) Two large cyclones, originating from a zone of cyclogenesis in Eastern Siberia, tracking over a large area of open water. (3) An overall decline in mean Arctic ice thickness, (4) a heavily decayed ('rotten') FY ice cover flanking the MY pack ice in the Southern Beaufort Sea with a calculated average flexural strength of 64.3 kPa, (5) Warm, nearly isothermal and low-strength MY ice coverage with a calculated average flexural strength of 40.9 kPa. These factors are driven by climate change, and are representative of a shift in the Arctic sea ice regime, from one characterized by a predominately MY ice cover, toward a new regime comprised of seasonal FY sea ice. The most striking result of this event is the large spatial extent over which fractured sea ice cover was observed, and represents a nearly instantaneous reduction in regional mean ice floe size, thereby affecting regional albedo values and surface energy budgets. The resulting smaller floes are highly susceptible to lateral melting and decay, especially when transported dynamically to the south and west in the Beaufort sea ice gyre where they are subject to increased solar radiation, to increased bottom melt from Pacific warm water intrusions, or advection of warmer surface mixed layer waters from open water areas, under the remnant pack ice.

[36] This event represents a new mechanical forcing mechanism upon sea ice cover in the Arctic Basin. Of note, this represents a positive feedback process that may accelerate the loss of sea ice cover, particularly during the summer months. We are convinced that events of this nature will continue to occur in future years, especially when large fetch emerges early in the melt season, and are bound to have implications for coastal erosion, transportation, and industrial activities in the Arctic Basin. Continued monitoring of the Arctic Basin is essential to better understanding new forms of ocean-sea ice-atmosphere interactions and coupling as they emerge in the coming seasonal Arctic sea ice regime. This process will have implications for modeling future sea ice dynamics and thermodynamics, and needs to be included in regional and large scale climate models to enhance processes of sea ice decay, formation and motion.

References

Barber, D. G., R. Galley, M. G. Asplin, R. De Abreu, K. A. Warner, M. Pućko, M. Gupta, S. Prinsenberg, and S. Julien (2009), Perennial pack ice in the southern Beaufort Sea was not as it appeared in the summer of 2009, *Geophys. Res. Lett.*, 36, L24501, doi:10.1029/2009GL041434.

Bearman, G. (1999), *Waves, Tides and Shallow-Water Processes*, 2nd ed., Butterworth-Heinemann, Oxford, U. K.

Bromwich, D. H., and S.-H. Wang (2005), Evaluation of the NCEP-NCAR and ECMWF 15- and 40-yr reanalyses using rawinsonde data from two independent Arctic field experiments, *Mon. Weather Rev.*, 133, 3562–3578, doi:10.1175/MWR3043.1.

Eicken, H., M. Lensu, M. Lepparanta, W. B. Tucker III, A. J. Gow, and O. Salmela (1995), Thickness, structure and properties of level summer multiyear ice in the Eurasian sector of the Arctic Ocean, *J. Geophys. Res.*, 100(C11), 22,697–22,710.

Frankenstein, G. E., and R. Garner (1967), Equations for determining the brine volume of sea ice from 0.5–22.9 C, *J. Glaciol.*, *6*, 943–944.

Higgins, M. E., and J. J. Cassano (2009), Impacts of reduced sea ice on winter Arctic atmospheric circulation, precipitation, and temperature, *J. Geophys. Res.*, *114*, D16107, doi:10.1029/2009JD011884.

Hilmer, M., and P. Lemke (2000), On the decrease of Arctic sea ice volume, *Geophys. Res. Lett.*, *27*(22), 3751–3754, doi:10.1029/2000GL011403.

Hunkins, K. (1962), Waves on the Arctic Ocean, *J. Geophys. Res.*, *67*, 2477–2489, doi:10.1029/JZ067i006p02477.

Intergovernmental Panel on Climate Change (2007), *Climate Change 2007: The Physical Science Basis: Contribution of Working Group I to the Fourth Assessment Report of the Intergovernmental Panel on Climate Change*, edited by S. Solomon et al., Cambridge Univ. Press, New York.

Kalnay, E., et al. (1996), The NCEP/NCAR 40-year reanalysis project, *Bull. Am. Meteorol. Soc.*, *77*, 437–471, doi:10.1175/1520-0477(1996)077<0437:TNYRP>2.0.CO;2.

Kwok, R., and G. F. Cunningham (2010), Contribution of melt in the Beaufort Sea to the decline in Arctic multiyear sea ice coverage: 1993–2009, *Geophys. Res. Lett.*, *37*, L20501, doi:10.1029/2010GL044678.

Kwok, R., G. F. Cunningham, M. Wensnahan, I. Rigor, H. J. Zwally, and D. Yi (2009), Thinning and volume loss of the Arctic Ocean sea ice cover: 2003–2008, *J. Geophys. Res.*, *114*, C07005, doi:10.1029/2009JC005312.

LeDrew, E. L., D. Johnson, and J. A. Maslanik (1991), An examination of atmospheric mechanisms that may be responsible for the annual reversal of the Beaufort Sea ice field, *Int. J. Clim.*, *11*, 841–859.

Liu, A. K., and E. Mollo-Christensen (1988), Wave propagation in a solid ice pack, *J. Phys. Oceanogr.*, *18*, 1702–1712, doi:10.1175/1520-0485(1988)018<1702:WPIASI>2.0.CO;2.

Markus, T., J. C. Stroeve, and J. Miller (2009), Recent changes in Arctic sea ice melt onset, freeze-up and melt season length, *J. Geophys. Res.*, *114*, C12024, doi:10.1029/2009JC005436.

Maslanik, J. A., C. Fowler, J. Stroeve, S. Drobot, J. Zwally, D. Yi, and W. Emery (2007), A younger, thinner Arctic ice cover: Increased potential for rapid extensive sea ice loss, *Geophys. Res. Lett.*, *34*, L24501, doi:10.1029/2007GL032043.

Maslanik, J., J. Stroeve, C. Fowler, and W. Emery (2011), Distribution and trends in Arctic sea ice age through spring 2011, *Geophys. Res. Lett.*, *38*, L13502, doi:10.1029/2011GL047735.

McLaren, A. S., M. C. Serreze, and R. G. Barry (1987), Seasonal variations of sea ice motion in the Canada Basin and their implications, *Geophys. Res. Lett.*, *14*, 1123–1126, doi:10.1029/GL014i011p01123.

Mellor, M. (1986), Mechanical behaviour of sea ice, in *The Geophysics of Sea Ice*, edited by N. Untersteiner, pp. 165–281, Plenum, New York.

Nghiem, S. V., I. G. Rigor, D. K. Perovich, P. Clemente-Colon, J. W. Weatherly, and G. Neumann (2007), Rapid reduction of Arctic perennial sea ice, *Geophys. Res. Lett.*, *34*, L19504, doi:10.1029/2007GL031138.

Ogi, M., K. Yamazaki, and J. Wallace (2010), Influence of winter and summer surface wind anomalies on summer Arctic sea ice extent, *Geophys. Res. Lett.*, *37*, L07701, doi:10.1029/2009GL042356.

Perovich, D. K., J. A. Richter-Menge, K. F. Jones, and B. Light (2008), Sunlight, water, and ice: Extreme Arctic sea ice melt during the summer of 2007, *Geophys. Res. Lett.*, *35*, L11501, doi:10.1029/2008GL034007.

Prinsenberg, S. J., and J. S. Holladay (1993), Using an air-borne electromagnetic ice-thickness sensor to validate remotely sensed marginal ice zone properties, in *Proceedings of the 12th International Conference on Port and Ocean Engineering Under Arctic Conditions, August 17–20, Hamburg (FRG)*, vol. 2, pp. 936–948, Hamburg Ship Model Basin, Hamburg, Germany.

Proshutinsky, A. Y., R. H. Bourke, and F. A. McLaughlin (2002), The role of the BG in Arctic climate variability: Seasonal to decadal climate scales, *Geophys. Res. Lett.*, *29*(23), 2100, doi:10.1029/2002GL015847.

Rothrock, D. A., and A. S. Thorndike (1984), Measuring the sea ice floe distribution, *J. Geophys. Res.*, *89*(C4), 6477–6486, doi:10.1029/JC089iC04p06477.

Rothrock, D. A., Y. Yu, and G. A. Maykut (1999), Thinning of the Arctic sea-ice cover, *Geophys. Res. Lett.*, *26*(23), 3469–3472, doi:10.1029/1999GL010863.

Screen, J., and I. Simmonds (2011), Declining summer snowfall in the Arctic: Causes, impacts and feedbacks, *Clim. Dyn.*, *38*(11–12), 2243–2256, doi:10.1007/s00382-011-1105-2.

Serreze, M. C., and R. G. Barry (1988), Synoptic activity in the Arctic Basin. 1979–85, *J. Clim.*, *1*, 1276–1295, doi:10.1175/1520-0442(1988)001<1276:SAITAB>2.0.CO;2.

Shimada, K., T. Kamoshida, M. Itoh, S. Nishino, E. Carmack, F. McLaughlin, S. Zimmermann, and A. Proshutinsky (2006), Pacific Ocean inflow: Influence on catastrophic reduction of sea ice cover in the Arctic Ocean, *Geophys. Res. Lett.*, *33*, L08605, doi:10.1029/2005GL025624.

Simmonds, I., and K. Keay (2009), Extraordinary September Arctic sea ice reductions and their relationships with storm behavior over 1979–2008, *Geophys. Res. Lett.*, *36*, L19715, doi:10.1029/2009GL039810.

Solheim, F., J. R. Godwin, E. R. Westwater, Y. Han, S. J. Keihm, K. March, and R. Ware (1998), Radiometric profiling of temperature, water vapor, and cloud liquid water using various inversion methods, *Radio Sci.*, *33*, 393–404, doi:10.1029/97RS03656.

Squire, V. A., G. L. Vaughan, and L. G. Bennetts (2009), Ocean surface wave evolvement in the Arctic basin, *Geophys. Res. Lett.*, *36*, L22502, doi:10.1029/2009GL040676.

Steele, M. (1992), Sea ice melting and floe geometry in a simple ice-ocean model, *J. Geophys. Res.*, *97*(C11), 17,729–17,738, doi:10.1029/92JC01755.

Steele, M., W. Ermold, and J. Zhang (2008), Arctic Ocean surface warming trends over the past 100 years, *Geophys. Res. Lett.*, *35*, L02614, doi:10.1029/2007GL031651.

Steer, A., A. Worby, and P. Heil (2008), Observed changes in sea-ice floe distribution during early summer in the Western Weddell Sea, *Deep Sea Res., Part II*, *55*, 933–942, doi:10.1016/j.dsr2.2007.12.016.

Stroeve, J. C., M. C. Serreze, F. Fetterer, T. Arbetter, W. Meier, J. Maslanik, and K. Knowles (2005), Tracking the Arctic's shrinking ice cover: Another extreme September minimum in 2004, *Geophys. Res. Lett.*, *32*, L04501, doi:10.1029/2004GL021810.

Stroeve, J. C., M. C. Serreze, M. M. Holland, J. E. Kay, J. Maslanik, and A. P. Barrett (2011a), The Arctic's rapidly shrinking sea ice cover: A research synthesis, *Clim. Change*, *110*(3–4), 1005–1027.

Stroeve, J. C., M. C. Serreze, A. Barrett, and D. Kindig (2011b), Attribution of recent changes in autumn cyclone associated precipitation in the Arctic, *Tellus, Ser. A*, *63*(4), 653–663, doi:10.1111/j.1600-0870.2011.00515.x.

Timco, G. W., and M. E. Johnston (2002), Sea ice strength during the melt season, Ice in the environment, paper presented at 16th IAHR International Symposium on Ice, Dunedin, New Zealand, 2–6 Dec.

Timco, G. W., and S. O'Brien (1994), Flexural strength equation for sea ice, *Cold Reg. Sci. Technol.*, *22*(3), 285–298, doi:10.1016/0165-232X(94)90006-X.

Tison, J. L., A. P. Worby, B. Delille, F. Brabant, S. Papadimitriou, D. Thomas, J. de Jong, D. Lannuzel, and C. Haas (2009), Temporal evolution of decaying summer first-year sea ice in the western Weddell Sea, Antarctica, *Deep Sea Res., Part II*, *55*(8–9), 975–987.

Toyota, T., S. Takatsuji, and M. Nakayama (2006), Characteristics of sea ice floe size distribution in the seasonal ice zone, *Geophys. Res. Lett.*, *33*, L02616, doi:10.1029/2005GL024556.

Wadhams, P. (1973), Attenuation of swell by sea ice, *J. Geophys. Res.*, *78*(18), 3552–3563, doi:10.1029/JC078i018p03552.

Wadhams, P., and M. J. Doble (2009), Sea ice thickness measurement using episodic infragravity waves from distant storms, *Cold Reg. Sci. Technol.*, *56*, 98–101, doi:10.1016/j.coldregions.2008.12.002.

Wadhams, P., A. E. Gill, and P. F. Linden (1979), Transects by submarine of the East Greenland Polar Front, *Deep Sea Res.*, *26A*, 1311–1327.

Wadhams, P., V. A. Squire, D. J. Goodman, A. M. Cowan, and S. C. Moore (1988), The attenuation of ocean waves in the marginal ice zone, *J. Geophys. Res.*, *93*, 6799–6818, doi:10.1029/JC093iC06p06799.

Woodgate, R. A., K. Aagaard, and T. J. Weingartner (2006), Interannual changes in the Bering Strait fluxes of volume, heat and freshwater between 1991 and 2004, *Geophys. Res. Lett.*, *33*, L15609, doi:10.1029/2006GL026931.

Zhang, X., J. E. Walsh, J. Zhang, U. S. Bhatt, and M. Ikeda (2004), Climatology and interannual variability of Arctic cyclone activity, 1948–2002, *J. Clim.*, *17*, 2300–2317, doi:10.1175/1520-0442(2004)017<2300:CAIVOA>2.0.CO;2.